# Aseismic deformation associated with an earthquake swarm in the northern Apennines (Italy)

A. Gualandi[a,1,*], C. Nichele[2], E. Serpelloni[3], L. Chiaraluce[3], L. Anderlini[3], D. Latorre[3], M.E. Belardinelli[2], J.-P. Avouac[1]

[a] *1200 East California Boulevard, MC 100-23, Pasadena, CA 91125, USA.*

---

## Contents of this file

## Introduction

In Section S1 we provide the completeness magnitude and $b$-value estimations for the catalog under study, together with the conversion of local magnitudes into moment magnitudes. In Section S2 we derive the lower and upper bounds for the moment released by the seismic swarm under the assumption that also non detected earthquakes follow the Gutenberg-Richter law. In Section S3 we describe the steps to obtain the GPS position time series. In Section S4 we give an overview of the variational bayesian Independent Component Analysis (vbICA) methodology adopted in this work to decompose the GPS position time series. In Section S5 we present the results of the inversion performed on the fourth Independent Component (IC$_4$) derived from the vbICA decomposition. In Section S6 we furnish an estimation of the range for the aseismic moment needed to explain the observed geodetic transient signal. The Figures S1 to S6 conclude this file.

## S1. $M_C$ and $b$-value

The frequency-magnitude distribution of earthquakes is shown in Figure S1a. From the Gutenberg-Richter (GR) law we estimate the time-dependent completeness magnitude $M_C$ for the overall catalog by applying the Goodness of Fit (GFT) and the Magnitude and B-value Stability (MBS) methods (Woessner and Wiemer, 2005), both based on the maximum likelihood

---

[*] Corresponding author
*Email address:* `gualandi@caltech.edu` (A. Gualandi)
[1] California Institute of Technology, Department of Geology and Planetary Sciences, Pasadena, CA, USA.
[2] University of Bologna, Dipartimento di Fisica e Astronomia, Settore di Geofisica, Italy.
[3] Istituto Nazionale di Geofisica e Vulcanologia, Italy.

*Preprint submitted to Geophysical Research Letters* *June 12, 2017*

estimation of the $b$-value. To balance the temporal evolution of seismicity with the number of events, we apply the GFT and MBS methods in overlapping time windows of one month, daily updated. The results are shown in Figure S1b.

The conversion from $M_L$ to $M_w$ is given by equation (11) of Munafó et al. (2016), that we report here:

$$M_w = \frac{2}{3}M_L + 1.15 \tag{S1}$$

and the inverse of it is:

$$M_L = \frac{3}{2}(M_w - 1.15) \tag{S2}$$

The $b$-value has been obtained from the GR law adopting the local magnitudes $M_L$. If we use the moment magnitudes $M_w$ instead we obtain:

$$\text{Log}N = a_L - b_L M_L = a_L - b_L\frac{3}{2}(M_w - 1.15) = a_L - 1.15\frac{3}{2}b_L - \frac{3}{2}b_L M_w = a_w - b_w M_w \tag{S3}$$

where we find that the GR law is still valid but the $b$-value is now $b_w = \frac{3}{2}b_L$. We are neglecting the uncertainties in the relation that converts $M_L$ into $M_w$, so the uncertainty on $b_w$ is just $\frac{3}{2}$ of the uncertainty on $b_L$. Since the GR law is still valid also when using $M_w$ after the conversion from $M_L$, we can convert the completeness magnitude $M_C$ into $M_{w\ C}$ just using equation S1.

## S2. Seismic moment lower and upper bounds

Let us consider the earthquakes in the space and time windows where geodetic and seismic data overlap, i.e. $\sim 30$ km from the barycenter of clustered seismicity and from 2012.0 to 2015.7566. In this Section we want to estimate lower and upper bounds for the seismic moment released during the seismic swarm.

A lower bound can be obtained ignoring the contribution of small earthquakes ($M_w < M_{w\ C}$) and considering only the clustered events with $M_w \geq M_{w\ C}$. This quantity is easy to be calculated, and it is $M_{0\ seismic}^{min} = [0.80 \pm 0.23] \times 10^{16}$ Nm, i.e. $M_w^{min} = 4.53 \pm 0.08$. The uncertainty on the cumulative seismic moment is calculated summing linearly the uncertainties on the moment of every single earthquake, that corresponds to an upper bound for the final uncertainty. From now on, all the uncertainties are estimated following the approach described in Taylor (1982), where calculations are carried retaining all available digits, and only the presented results are rounded to the significant figures.

An upper bound for the seismic moment associated with the swarm activity ($M_{0\ seismic}^{max}$) can be calculated summing: 1) $M_{0\ seismic}$ for clustered events having $M_w \geq M_{w\ C}$ (i.e., $M_{0\ seismic}^{min}$), 2) the upper limit of the seismic moment for small earthquakes under the hypothesis that the GR relation holds with the same $b$-value also for $M_w < M_{w\ C}$ (e.g., Gualandi et al., 2016b).

1) The seismic moment released by clustered earthquakes with $M_w \geq M_{w\ C}$ is the lower bound mentioned above: $M_{0\ seismic}^{min} = [0.80 \pm 0.23] \times 10^{16}$ Nm.

2) If we have $N_1$ earthquakes with magnitude larger or equal to $M_{w\ 1}$, and $N_2 > N_1$ earthquakes with magnitude larger or equal to $M_{w\ 2} < M_{w\ 1}$, we can express an overestimation of the seismic moment produced by the earthquakes with magnitude in the range $M_{w\ 2} \leq M_w \leq M_{w\ 1}$ using equation (B6) of Gualandi et al. (2016b):

$$\nu_{1,2} = M_{0*} N_*^{\frac{3}{2b_w}} \frac{2b_w}{2b_w - 3} N^{\frac{2b_w-3}{2b_w}} \Big|_{N_1}^{N_2} \tag{S4}$$

where we select for $M_{0*} = M_{0\ C} = 2.69 \times 10^{11}$ Nm, i.e. the moment associated with an earthquake of magnitude $M_{w\ C}$, and $N_*$ is the number of earthquakes in the catalog with $M_w \geq M_{w\ C}$.

To evaluate the upper bound to the moment released by earthquakes with $M_w < M_{w\ C}$ means to take $N_1 = N_*$ and $N_2 \to \infty$:

$$\nu_{1,2} = M_{0*} N_*^{\frac{3}{2b_w}} \frac{2b_w}{2b_w - 3} \left(N_2^{\frac{2b_w-3}{2b_w}} - N_1^{\frac{2b_w-3}{2b_w}}\right) \tag{S5}$$

We see that for $b_w \geq 1.5$, $\nu_{1,2}$ diverges. In our case $b_w = 1.440 \pm 0.015 < 1.5$, and the integral S4 is well behaved. The term with $N_2$ tends towards 0, and we have:

$$\nu_{1,2} = -M_{0*} N_*^{\frac{3}{2b_w}} \frac{2b_w}{2b_w - 3} N_*^{\frac{2b_w-3}{2b_w}} = -\frac{2b_w}{2b_w - 3} M_{0*} N_* \tag{S6}$$

For the clustered events we have $N_* = 3696$. Plugging $M_{0\ *}$ and $N_*$ values into equation S6, and using the $b_w$-value from Section S1, we obtain $\nu_{1,2} = [0.64 \pm 0.17] \times 10^{16}$ Nm. The uncertainty has been obtained propagating only the uncertainty on $b_w$:

$$\delta\nu_{1,2} = \left|\frac{\partial \nu_{1,2}}{\partial b_w}\right| \delta b_w = \left| -\frac{6}{(2b_w - 3)^2} M_{0\ *} N_* \right| \delta b_w = \frac{6}{(2b_w - 3)^2} M_{0\ *} N_* \delta b_w \tag{S7}$$

If we sum this upper bound to the moment calculated for the clustered earthquakes with $M_w \geq M_{w\ C}$ we obtain:

$$M_{0\ seismic}^{max} = \nu_{1,2} + M_{0\ seismic}^{min} = [0.64 \pm 0.17] \times 10^{16}\ \text{Nm} + [0.80 \pm 0.23] \times 10^{16}\ \text{Nm} = [1.44 \pm 0.29] \times 10^{16}\ \text{Nm} \tag{S8}$$

where the uncertainty is the square root of the sum of the squares of the uncertainties. This value is the same reported in Section 3.1.

## S3. Derivation of GPS position time series

The position time-series have been obtained adopting a three-step procedure approach, as in Serpelloni et al. (2006), that includes 1) raw phase data reduction, 2) combination of loosely-constrained solutions and reference frame definition, and 3) estimation of long-term linear trend and Common Mode Error (CME).

The raw GPS observables have been analyzed using the 10.6 version of the GAMIT/GLOBK package (Herring et al., 2015) adopting standards defined in the framework of the IGS "Repro2 campaign" (`http://acc.igs.org/reprocess2.html`). The GAMIT software is used to estimate station positions, atmospheric delays, satellite orbits, and Earth orientation parameters from ionosphere-free linear combination GPS phase observables using double differencing techniques to eliminate phase biases caused by drifts in the satellite and receiver clock oscillators. GPS pseudo-range observables are used to constrain clock timing offsets and to improve automated editing of the phase data, assisting in the resolution of integer phase ambiguities. GPS phase data are weighted according to an elevation-angle-dependent error model (Herring et al., 2015) using an iterative analysis procedure whereby the elevation dependence is determined from the observed scatter of phase residuals.

In this analysis the satellites orbit parameters are fixed to the IGS final products. We use the IGS absolute antenna phase center model for both satellite and ground-based antennas, which improves the accuracy of estimates for the vertical components of site position by mitigating reference frame scale and atmospheric mapping function errors (e.g., Schmid et al., 2005, 2007). While the first-order ionospheric delay is eliminated by the ionosphere-free linear combination, the second-order ionospheric corrections are applied based on the formulation of Petrie et al. (2010), using IONEX files from the Center for Orbit Determination in Europe (CODE). The tropospheric delay is modeled as piecewise linear model and estimated using the Vienna Mapping Function 1 (VMF1; Boehm et al., 2006) mapping function with a 10° cutoff. We use the Global Pressure and Temperature 2 (GPT2; Lagler et al., 2013) model to provide a priori hydrostatic delays. The pole tide was also corrected in GAMIT by IERS standards. The Earth Orientation Parameters (EOP) are tightly constrained to priori values obtained from IERS Bulletin B. Non-tidal atmospheric loading and ocean tidal loading are corrected using MIT filtered atmospheric displacements files (available at `ftp://everest.mit.edu/pub/GRIDS`) and the FES2004 (Lyard et al., 2006) model, respectively. The International Earth Rotation Service (IERS) 2003 model for diurnal and semi-diurnal solid Earth tides was set. Because of the large number of stations included in our Euro-Mediterranean GPS processing ($\sim 3000$), this step is performed for several sub-networks, each made by $< 50$ stations, with each sub-network sharing a set of high-quality IGS stations, which are used as tie-stations in the combination step.

In the second step we use the ST_FILTER program of the QOCA software (`http://qoca.jpl.nasa.gov`), which adopts a Kalman filter estimation algorithm (Dong et al., 1998, 2002), to combine all the daily loosely constrained solutions with the global solution of the IGS network made available by MIT (`http://sopac.ucsd.edu`), and simultaneously realize a global reference frame by applying generalized constraints (Dong et al., 1998). Specifically, we define the reference frame by minimizing the velocities of the IGS core stations (`http://igscb.jpl.nasa.gov`), while estimating a seven-parameter transformation with respect to the GPS realization of the ITRF2008 frame (Altamimi et al., 2011), i.e., the IGb08 reference frame. In the third step we analyze the position time series in order to estimate and correct offsets due to stations equipment changes, while simultaneously estimating annual and semi-annual periodic signals and a linear velocity term. In this analysis we retain only data from GPS stations with an observation period longer than 2.5 years, as shorter intervals may result in biased estimates of linear velocities (Blewitt and Lavallée, 2002). The model derived from the combination of these signals is then subtracted from the position time series in order to get the residual positions. The residual time-series are then used to estimate the Common Mode Error (CME) performing a Principal Component Analysis (PCA), as described in Dong et al. (2006). The PCA is performed at a continental-scale, over the same area used by Serpelloni et al. (2013), and the first two PCs are here considered as CME. This prevents the removal of the eventual more localized signals of geophysical interests recorded by the GPS stations in the study region, since the PCA detects the signals common to a much larger region. As a result, after removing the CME, the typical repeatability in our analysis is $\sim 1$ mm for the horizontal components, and $\sim 3$ mm for the vertical component, with a 30% gain in the daily repeatability and a significant improvement of the signal to noise ratio. After the spatial filtering, the estimated seasonal motions are added back to the filtered time-series, obtaining position time series with a reduced scatter around the adopted model.

The position time series of the 15 cGPS stations used to study the transient signal are available in the files `*_GPS.resi.cgps_atf_raw_det_nooff.flt.wrmsx3.100km.umbe`. The columns are organized as follows:

1. Epoch (decimal yr)
2. East position (mm)
3. North position (mm)
4. Uncertainty in the East position (mm)
5. Uncertainty in the North position (mm)
6. Correlation between East and North position (mm)
7. Up position (mm)
8. Uncertainty in the up position (mm)
9. Correlation between East and up position (mm)
10. Correlation between North and up position (mm)
11. Site name
12. Longitude (decimal degrees)
13. Latitude (decimal degrees)

## S4. Decomposition technique

The GPS position time series linear decomposition is performed following the variational Bayesian ICA (vbICA) approach. Differently from more standard ICA techniques, like FastICA (Hyvärinen and Oja, 1997), that are based on the so-called mapping approach, the vbICA relies on the so-called modelling approach. In both cases a cost function is built, and since the actual sources are unknown some approximations are introduced. The mapping approach approximations are usually based on the definition of mutual information or negentropy (e.g., Comon, 1994; Hyvärinen and Oja, 2000). The modelling approach instead creates a generative model, and looks for the model parameters that allow the data to be better explained while maintaining the sources as much statistically independent as possible. The cost function is based on the likelihood or, in a Bayesian framework, the posterior probability density function of the parameters. The modelling approach allows for more flexibility (i.e., a better representation of the original sources) and to take into account missing data in a consistent manner. Since in GPS measurements we often have gaps in the recording, we adopt a modified version of the multivariate statistical tool proposed by Choudrey and Roberts (2003), where the missing data are considered following the approach of Chan et al. (2003).

For every source we use a mix of four Gaussian distributions. The a priori hyperparameters that optimize the Negative Free Energy (NFE) associated with the generative model are reported in Table S3. The number of ICs retained is derived from an Automatic Relevance Determination (ARD) criterion and the study of the NFE. We adopt the same notation used in Gualandi et al. (2016a), where the temporal evolution of the Independent Components (ICs) is indicated by the columns of the matrix $V$, while the spatial distribution is associated with the corresponding columns of the matrix $U$. These two matrices have unit norm columns but, differently from a PCA, they have not orthogonal columns. A simple linear recombination of $U$ and $V^T$, with weighting factors expressed by the values of the diagonal matrix $S$, allows us to reconstruct the observed displacements at the surface $X$:

$$X \simeq USV^T \tag{S9}$$

where the approximation is due to the hypothesis that only few ICs are necessary to explain satisfactorily the geodetic observations, excluding eventual noise from the reconstruction. For further details on the vbICA algorithm we refer to Gualandi et al. (2016a) and references therein.

## S5. Inversion

In order to evaluate which structures are necessary to explain the data, we first run an inversion using $4 \times 4$, $2 \times 2$, and $2 \times 2$ patches along the strike and dip directions for the ATF, synthetic, and antithetic faults, respectively, and fixing the rake to be $-90°$. The number of parameters to be estimated is thus equal to the number of patches $P$ on which we retrieve the IC of slip (Table S5, column 3). Being the number of parameters ($P = 16 + 4 + 4 = 24$) less than the number of inverted data ($3 \times N_{GPS} = 45$) we can find the least square solution to the problem. We weight the solution using the nominal uncertainties $\sigma_{U_{IC_4}}$ derived from the vbICA analysis on $U_{IC_4}$. For every geometry configuration we estimate the misfit to the data ($\chi^2$, Table S5, column 2). We perform an $F$-test for every possible couple of nested models in order to verify if more complex models are justified by the data or not (Table S6). The null hypothesis is that the unrestricted model (model 2) does not provide a significantly better fit than the restricted model (model 1). We reject the null hypothesis if $F_{calculated} \geq F_{theoric}$. The results indicate that, at a significance level of 0.05, the model that uses both the synthetic and antithetic faults is significantly better then the models that use the synthetic or antithetic fault alone. Instead, at the same significance level, we have to reject the hypothesis that including the ATF is significantly improving the fit to the data with respect to the geometry that includes the synthetic and antithetic faults. We conclude that, even if the model with all the fault structures is the one with the lowest misfit, the displacement signal related to the inverted IC can be explained by slip on the synthetic and antithetic faults alone (Figure S4b), i.e. by deformation taking place in the ATF hanging wall.

## S6. $M_{0\ aseismic}$ bounds

Using the upper bound $M_{0\ seismic}^{max} = [1.44 \pm 0.29] \times 10^{16}$ Nm (Section S2), we obtain that the moment associated with aseismic deformation has the following lower bound:

$$\begin{aligned}\gamma M_{0\ seismic} = M_{0\ aseismic} \geq M_{0\ aseismic}^{min} = M_{0\ geodetic} - M_{0\ seismic}^{max} = \\ = [2.45 \pm 0.22] \times 10^{16}\ \text{Nm} - [1.44 \pm 0.29] \times 10^{16}\ \text{Nm} = \\ = [1.0 \pm 0.4] \times 10^{16}\ \text{Nm} = [70 \pm 29]\% M_{0\ seismic}^{max} = \gamma^{min} M_{0\ seismic}^{max}\end{aligned} \quad \text{(S10)}$$

If we consider only the clustered seismicity having $M_w \geq M_{w\ C}$ we obtain the upper bound:

$$\begin{aligned}\gamma M_{0\ seismic} = M_{0\ aseismic} \leq M_{0\ aseismic}^{max} = M_{0\ geodetic} - M_{0\ seismic}^{min} = \\ = [2.45 \pm 0.22] \times 10^{16}\ \text{Nm} - [0.80 \pm 0.23] \times 10^{16}\ \text{Nm} = \\ = [1.6 \pm 0.3] \times 10^{16}\ \text{Nm} = [200 \pm 70]\% M_{0\ seismic}^{min} = \gamma^{max} M_{0\ seismic}^{min}\end{aligned} \quad \text{(S11)}$$

where $2.45 - 0.80$ is rounded to 1.6 because the calculations are carried retaining all available digits ($2.4463... - 0.80397...$), and only the presented results are rounded to the significant figures, as in Taylor (1982).

## Bibliography

Z. Altamimi, X. Collilieux, and L. Metivier. ITRF2008: an improved solution of the International Terrestrial Reference Frame. *Journal of Geodesy*, 8(85):457–473, 2011. doi: 10.1007/s00190-011-0444-4.

G. Blewitt and D. Lavallée. Effect of annual signals on geodetic velocity. *Journal of Geophysical Research*, 107(B7,2145), 2002. doi:10.1029/2001JB000570.

J. Boehm, B. Werl, and H. Schuh. Troposphere mapping functions for GPS and very long baseline interferometry from European Centre for Medium-Range Weather Forecasts operational analysis data. *Journal of Geophysical Research*, 111 (B2), 2006. doi:10.1029/2005JB003629.

K. Chan, T.-W. Lee, and T.J. Sejnowski. Variational Bayesian Learning of ICA with Missing Data. *Neural Computation*, 15 (8):1991–2011, 2003.

R.A. Choudrey and S.J. Roberts. Variational Mixture of Bayesian Independent Component Analyzers. *Neural Computation*, 15(1):213–252, 2003.

P. Comon. Independent component analysis, A new concept? *Signal Processing*, 36:287–314, 1994.

D. Dong, T.A. Herring, and R.V. King. Estimating regional deformation from a combination of space and terrestrial geodetic data. *Journal of Geodesy*, (72):200–214, 1998.

D. Dong, P. Fang, Y. Bock, M.K. Cheng, and S. Miyazaki. Anatomy of apparent seasonal variations from GPS-derived site position time series. *Journal of Geophysical Research Solid Earth*, 107, 2002. doi: 10.1029/2001JB000573.

D. Dong, P. Fang, Y. Bock, F. Webb, L. Prawirodirdjo, S. Kedar, and P. Jamason. Spatiotemporal filtering using principal component analysis and Karhunen-Loeve expansion approaches for regional GPS network analysis. *Journal of Geophysical Research Solid Earth*, 111(B3), 2006. doi: 10.2029/2005JB003806.

A. Gualandi, E. Serpelloni, and M.E. Belardinelli. Blind source separation problem in GPS time series. *J. Geodesy*, 90(4): 323–341, 2016a. doi:10.1007/s00190-015-0875-4.

A. Gualandi, J. P. Avouac, J. Galetzka, J.F. Genrich, G. Blewitt, L.B. Adhikari, B.P. Koirala, R. Gupta, B.N. Upreti, B. Pratt-Sitaula, and J. Liu-Zeng. Pre- and post-seismic deformation related to the 2015, $\mathcal{M}_w$7.8 Gorkha Earthquake, Nepal. *Tectonophysics*, 2016b. http://dx.doi.org/10.1016/j.tecto.2016.06.014.

T.A. Herring, R.W. King, M.A. Floyd, and S.C. McClusky. *Introduction to GAMIT/GLOBK, Release 10.6*. Massachusetts Institute of Technology, 2015. http://www-gpsg.mit.edu/∼simon/gtgk/Intro_GG.pdf.

A. Hyvärinen and E. Oja. A fast fixed-point algorithm for Independent Component Analysis. *Neural Computation*, 9(7): 1483–1492, 1997.

A. Hyvärinen and E. Oja. Independent Component Analysis: Algorithms and Applications. *Neural Networks*, 13(4-5): 411–430, 2000.

K. Lagler, M. Schindelegger, J. Böhm, H. Krásná, and T. Nilsson. GPT2: Empirical slant delay model for radio space geodetic techniques. *Geophysical Research Letters*, 40:1069–1073, 2013. doi:10.1002/grl.50288.

F. Lyard, F. Lefevre, T. Letellier, and O. Francis. Modelling the global ocean tides: Modern insights from FES2004. *Ocean Dynam.*, 56:394–415, 2006.

I. Munafó, L. Malagnini, and L. Chiaraluce. On the Relationship between $M_w$ and $M_L$ for Small Earthquakes. *BSSA*, 106 (5):2402–2408, 2016. doi:10.1785/0120160130.

E.J. Petrie, M.A. King, P. Moore, and D.A. Lavallée. Higher-order ionospheric effects on the GPS reference frame and velocities. *J. Geophys. Res. Solid Earth*, 115(B3), 2010. doi:10.1029/2009JB006677.

R. Schmid, M. Rothacher, D. Thaller, and P. Steigenberger. Absolute phase center corrections of satellite and receiver antennas. *GPS Solut*, 9(4):283–293, 2005. doi:10.1007/s10291-005-0134-x.

R. Schmid, P. Steigenberger, G. Gendt, M. Ge, and M. Rothacher. Generation of a consistent absolute phase-center correction model for GPS receiver and satellite antennas. *J. Geod.*, 81(12):781–798, 2007. doi:10.1007/s00190-007-0148-y.

E. Serpelloni, G. Casula, A. Galvani, M. Anzidei, and P. Baldi. Data analysis of permanent GPS networks in Italy and surrounding regions: application of a ditributed processing approach. *Annals of Geophysics*, 49(4/5), 2006.

E. Serpelloni, C. Faccenna, G. Spada, D. Dong, and S.D.P. Williams. Vertical GPS ground motion rates in the Euro-Mediterranean region: New evidence of velocity gradients at different spatial scales along the Nubia-Eurasia plate boundary. *Journal of Geophysical Research: Solid Earth*, 118(11):6003–6024, 2013. doi: 10.1002/2013JB010102.

J.R. Taylor. *An Introduction to Error Analysis - The study of uncertainties in physical measurements.* University Science Books, Sausalito, California, 2nd edition, 1982.

J. Woessner and S. Wiemer. Assessing the quality of earthquake catalogues: Estimating the magnitude of completeness and its uncertainty. *Bulletin of the Seismological Society of America*, 95(2):684–698, 2005.

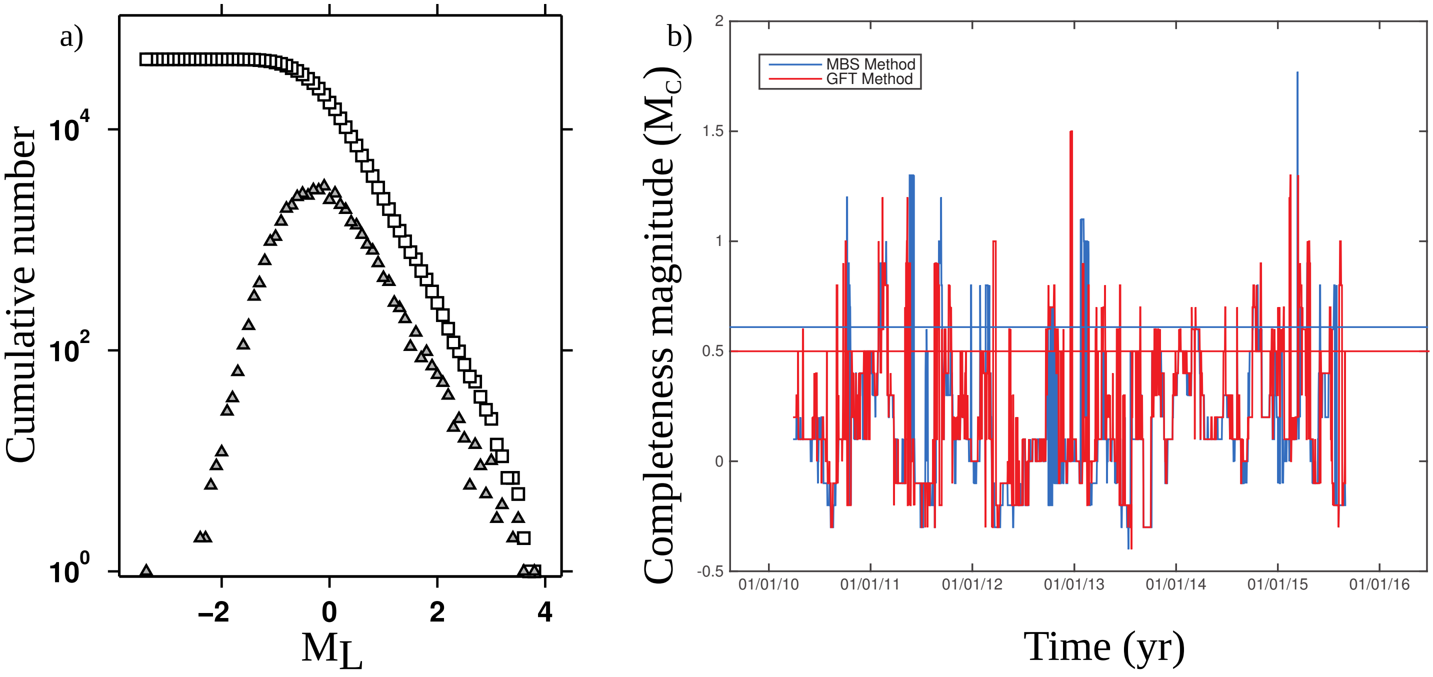

Figure S1: **a**): Squares: GR plot for the seismic catalog described in Section 3.1. Triangles: Number of earthquakes for every 0.1 binned magnitude. **b**): Time-dependent completeness magnitude $M_C$. Horizontal lines: average $M_C$, equal to 0.5 and 0.6 for the GFT and MBS methods, respectively. These $M_C$ values represent an underestimation in the first hours after the occurrence of the relatively strongest events but for the vast majority of the analyzed time window they are more than conservatives. The related $b$-values are $[0.95 \pm 0.01]$ and $[0.96 \pm 0.01]$. The two methods essentially give consistent results for most of the time intervals. To be conservative, in the calculations presented in the main text we used $M_C = 0.6$ and the corresponding $b_L = [0.96 \pm 0.01]$.

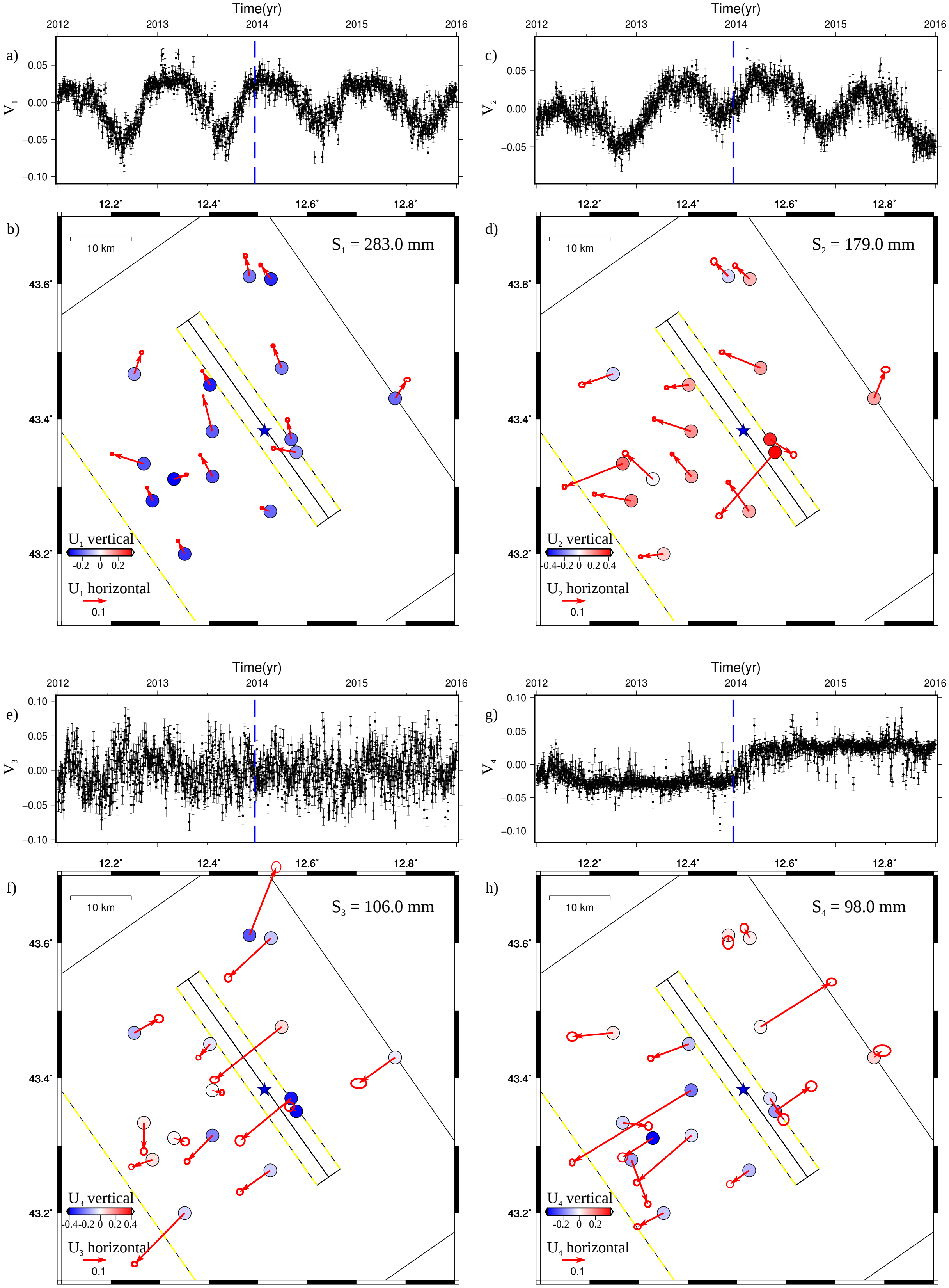

Figure S2: **a**), **c**), **e**), and **g**): Temporal evolution ($V$) of the four ICs, respectively, obtained performing a decomposition of the GPS position time series. Vertical blue dashed line: Time of the largest earthquake in the catalog. **b**), **d**), **f**), and **h**): Spatial distribution ($U$) of the four ICs. The weight $S$ is also reported (Section 3.2). Black boxes: Tested fault planes (ATF, synthetic, and antithetic) on which the $IC_4$ has been inverted (Section 4). Yellow dashed lines: Top edge of the fault planes. Blue star: Largest event in the seismic catalog.

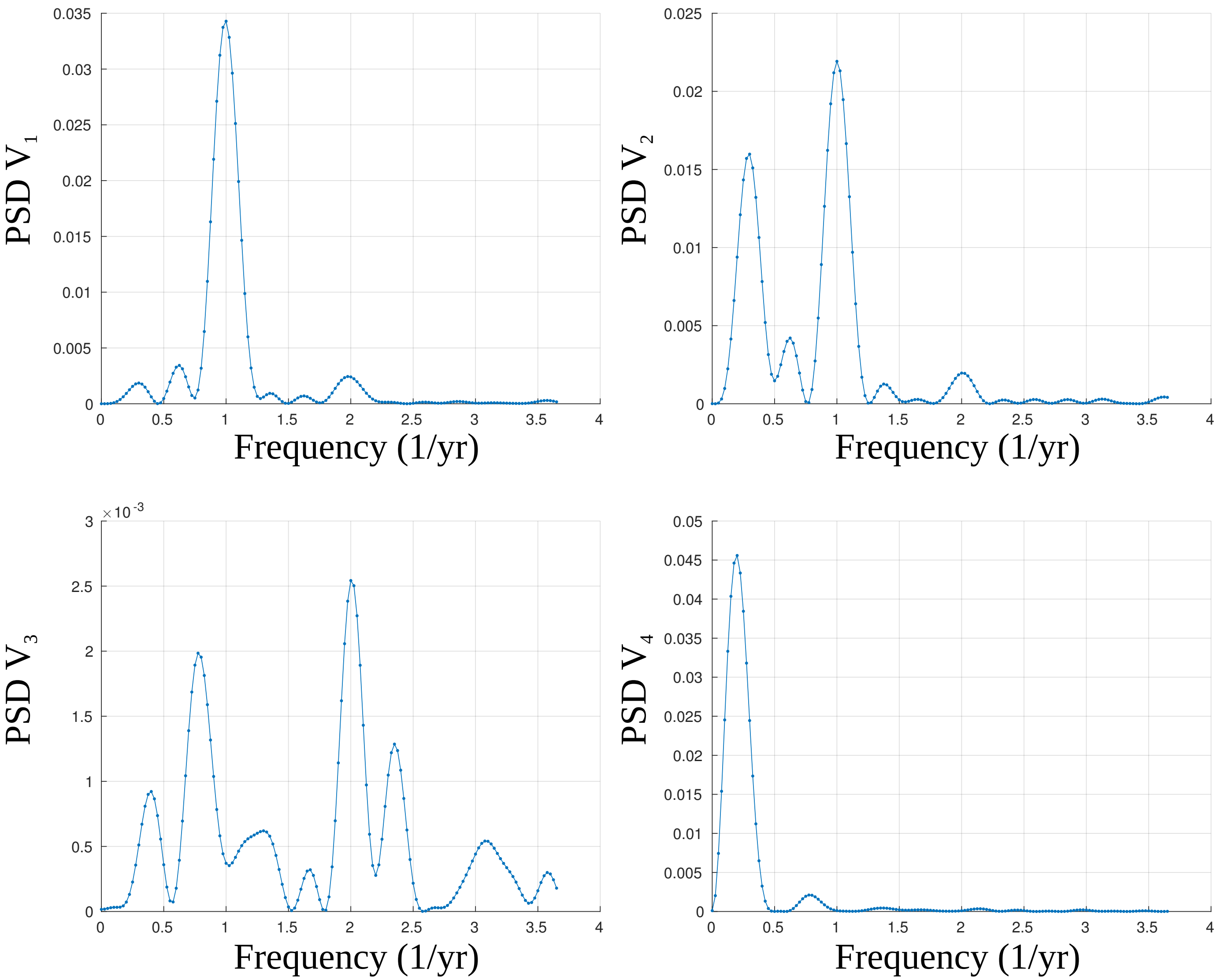

Figure S3: Power Sepctral Density (PSD) of the temporal functions $V$. For the first three ICs peaks at 1 and 2 1/yr are observed.

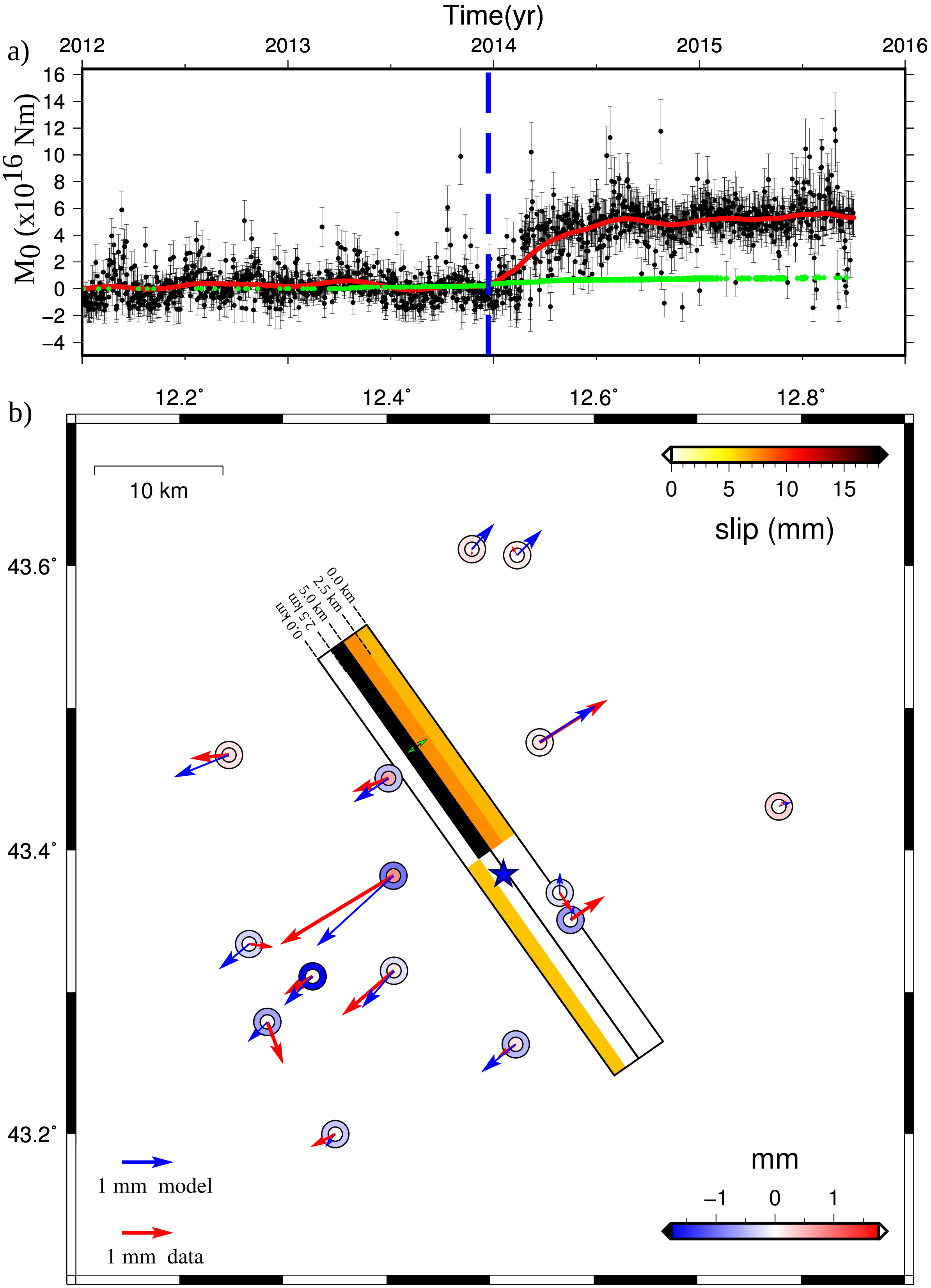

Figure S4: **a**: Black: Total (seismic + aseismic) cumulative moment released as derived from the slip model of panel **b assuming a rigidity modulus of 30 GPa**. The zero is set to the median of the first year of data. Red: low-pass zero-phase filter of total cumulative moment obtained with a moving window of 90 days. Green: cumulative seismic moment for clustered events with $M_w \geq M_{w\,C}$. **b**: Color palette: Cumulative slip of the model derived on large patches imposing a fixed rake of $-90°$. Fault boxes as in Figure 3. Black dashed lines: Faults' depth. Green arrows: rake direction for patches with slip $> 30\%$ of maximum slip. Red vectors/outer circles: horizontal/vertical cumulative displacement associated with $IC_4$. Blue vectors/inner circles: horizontal/vertical cumulative displacement associated with slip model.

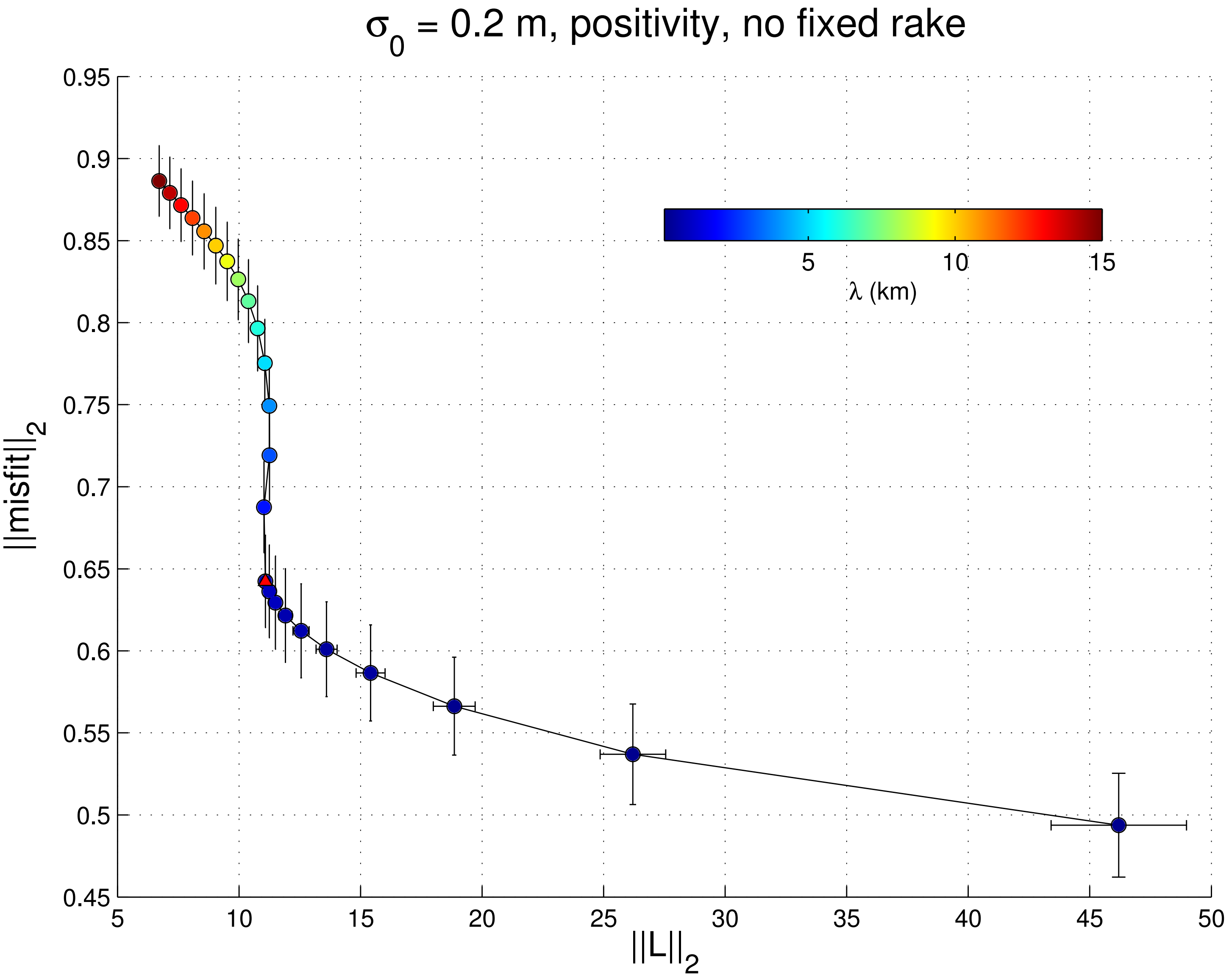

Figure S5: L-curve plot. On the x-axis the $L_2$ norm of the model $L$ obtained from the inversion of the linear system $U_{IC_4} = GL$, where $G$ is the matrix containing the Greens' functions; on the y-axis the $L_2$ norm of the misfit between the spatial distribution of the inverted IC and the predicted value from the model. Both quantities are non-dimensional. Color scale: Different results changing the smoothing parameter $\lambda$, ranging from 0.1 km to 15 km. Red triangle: Selected value for the best model, corresponding to $\lambda = 1$ km. All calculations have been performed with an assumed standard deviation on the a priori model parameters $\sigma_0 = 0.2$ m.

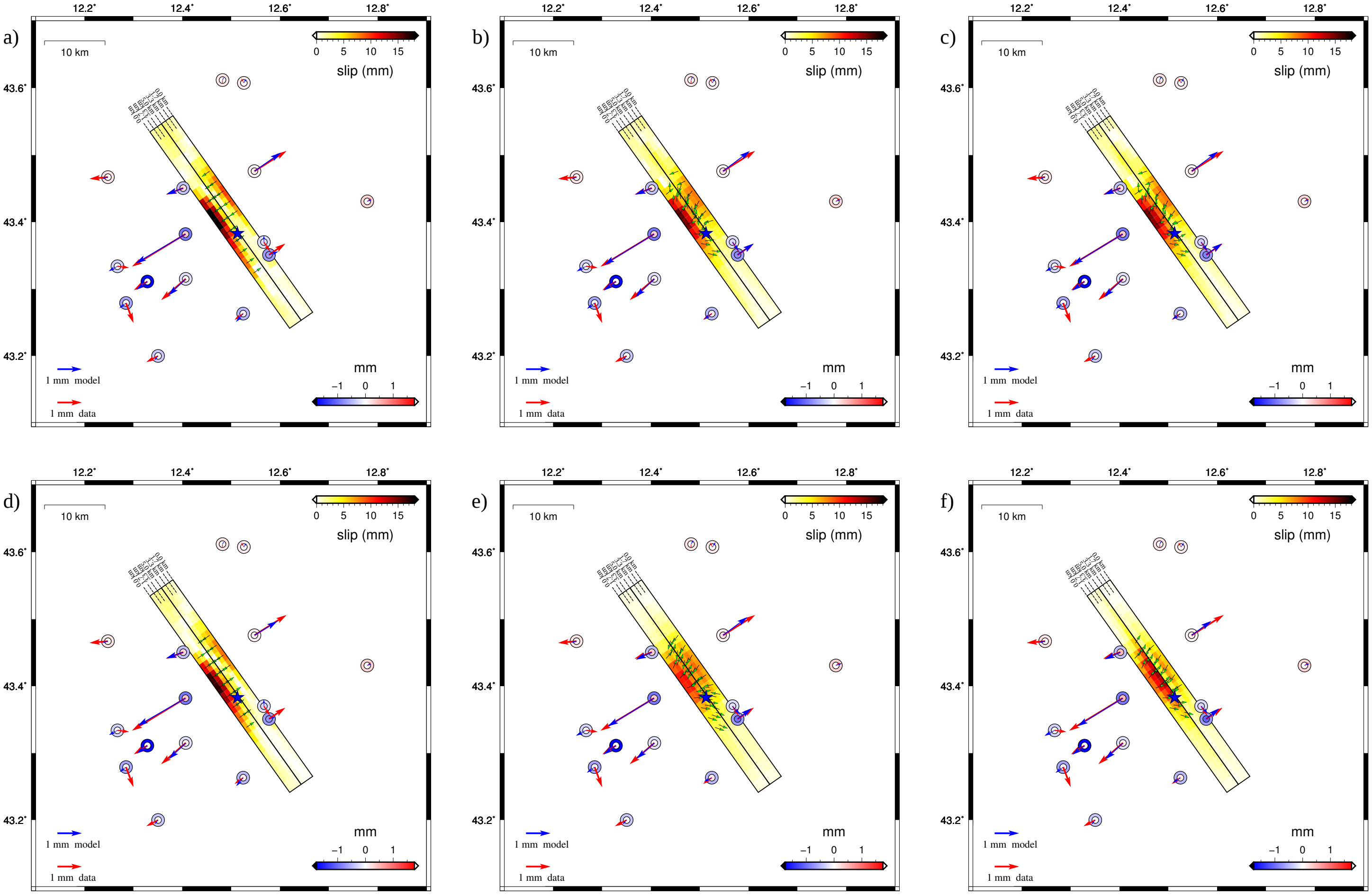

Figure S6: As Figure 4c, but for different inversion parameters. **a**: Fixed rake solution with $\sigma_0 = 0.2$ m and $\lambda$ as smoothing parameter. **b**: Variable rake solution with $\sigma_0 = 0.2$ m and $\lambda$ as smoothing parameter. **c**: Variable rake and positivity constraint solution with $\sigma_0 = 0.2$ m and $\lambda$ as smoothing parameter. Equivalent to Figure 4c. **d**: Fixed rake solution with $\lambda = 2$ km and $\sigma_0$ as smoothing parameter. **e**: Variable rake solution with $\lambda = 2$ km and $\sigma_0$ as smoothing parameter. **f**: Variable rake and positivity constraint solution with $\lambda = 2$ km and $\sigma_0$ as smoothing parameter.

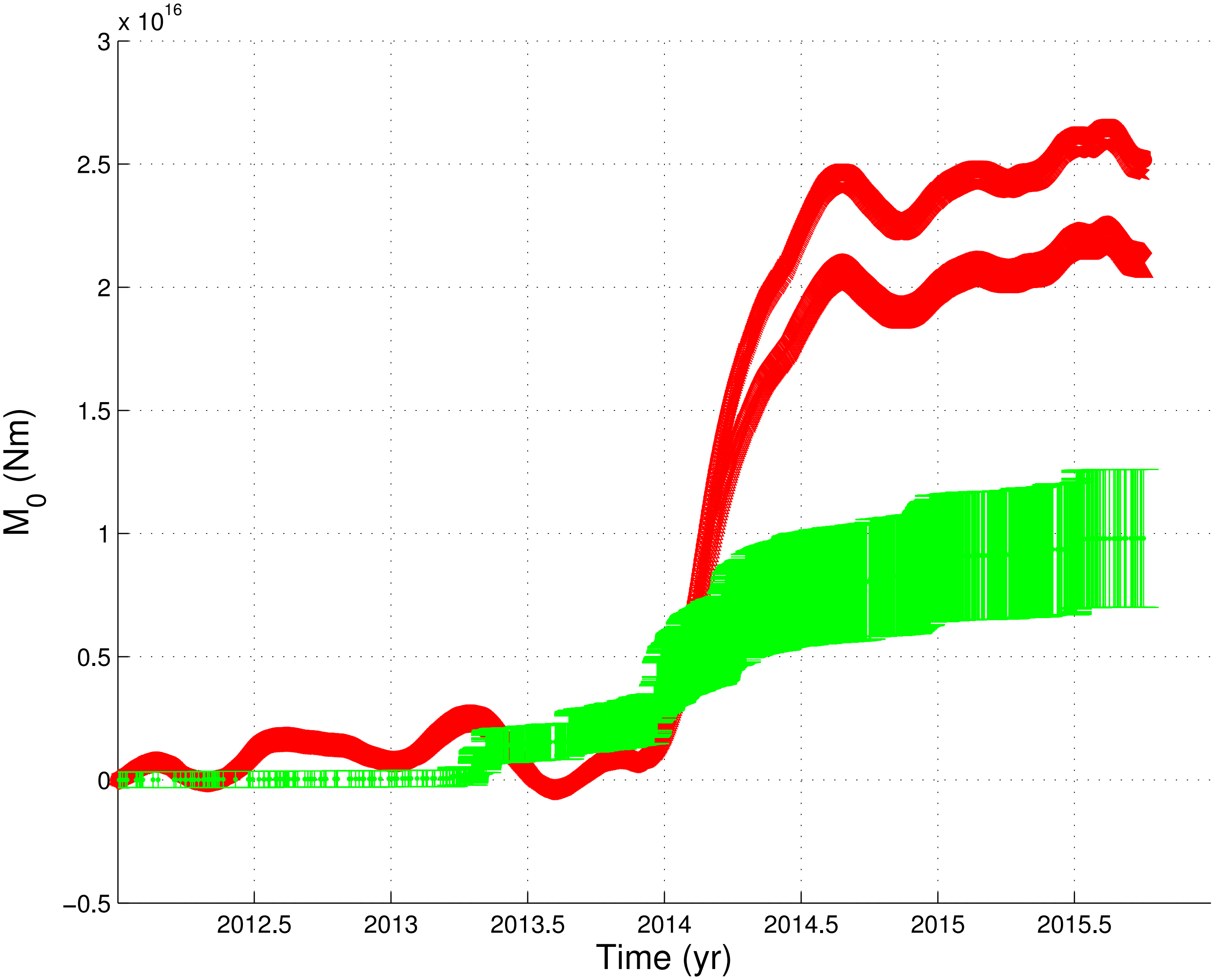

Figure S7: Red lines: Moment associated with the six models shown in Figure S6. Green: Seismic moment as in Figure 4b.